Journal of Materials Chemistry A

Accepted Manuscript

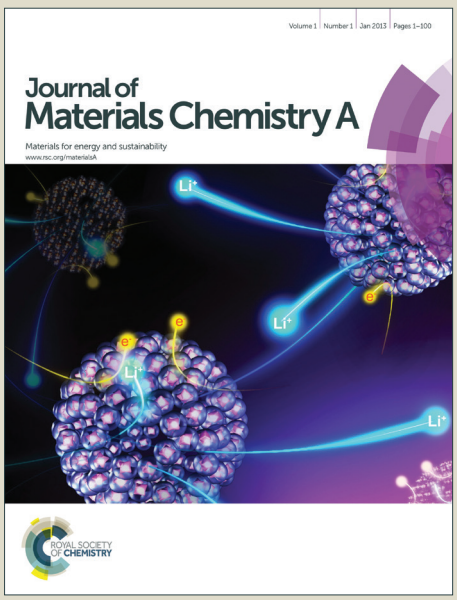

ROYAL SOCIETY OF CHEMISTRY

www.rsc.org/materialsA

Table of content

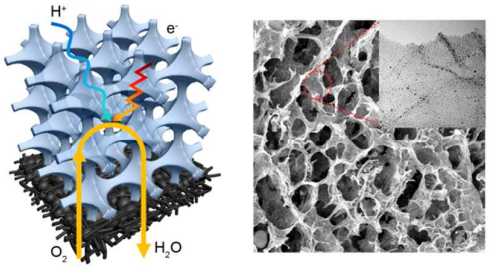

Newly designed electrode architecture based on Pt/graphene-Nafion® composite macroporous scaffold demonstrating ultra-high Pt utilization and superior fuel cell performance is presented.

Journal of Materials Chemistry A RSCPublishing

ARTICLE

Rational Design of a Highly Efficient Pt/Graphene-Nafion® Composite Fuel Cell Electrode Architecture

Cite this: DOI: 10.1039/x0xx00000x

Zhangxun Xia,[ab] Suli Wang,[a] Luhua Jiang,[a] Hai Sun,[a] Fulai Qi,[ab] Jutao Jin,[a] and Gongquan Sun[a]*

Received 00th January 2012,
Accepted 00th January 2012

DOI: 10.1039/x0xx00000x

www.rsc.org/

High platinum requirements hamper the commercialization and wide adoption of polymer electrolyte membrane fuel cells (PEMFCs). Hence, it is desirable to develop advanced electrode architecture which utilizes Pt more effectively than current designs. Herein, a novel electrode architecture based on Pt/graphene-Nafion® composite macroporous scaffold, prepared *via* facile freeze-drying approach, and demonstrating ultra-high Pt utilization is presented. Within the electrode architecture, pores act as gas/liquid transport channels while Nafion® ionomers act as proton carriers and graphene sheets allow conductance of electrons. By leveraging these tailored pathways for both mass and charges, a PEMFC prepared with this electrode architecture demonstrated superior performance, with a peak power density of 0.93 W cm^{-2} and cathode mass specific power density of 6.2 W mg^{-1}_{Pt}. These values are 6-fold greater than those produced using a lamellar structure with the same mass loading of Pt/graphene-Nafion® and also 1.2-fold greater than commercial Pt/C coated electrodes with the same Pt loading.

Introduction

PEMFCs are one of the most promising candidates for a new generation of energy technologies, and have recently neared the point of commercialization[1, 2]. However, their extensive use of Pt limits the general adoption of fuel cell-powered devices. Although the use of porous electrodes in PEMFCs represented a significant breakthrough in the 1990s as it considerably increased the efficiency of Pt utilization[3, 4], the state of the art still requires large amounts of Pt due to phenomena such as slow migration of charges (electrons or protons) or poor mass transfer of oxygen or water in the electrode. For PEMFCs made with carbon supported Pt nanoparticles (NPs), the most commonly-used cathode material, and using oxygen as the oxidant, the reduction of oxygen takes place only at or near the triple phase boundaries (TPBs), where both charges and mass may undergo rapid motion within the electrode[5, 6]. As such, tailored electrode architectures have been developed in order to increase the utilization of Pt[7]. These highly-efficient electrode architectures require high electron conductance through the supporting material, fast proton migration around the catalyst, and rapid mass transport through the channels of the electrode. Additionally, the hybrid pathways for charges and mass must be efficiently coupled in order to form TPBs. Optimized Pt utilization may be achievable by combining these features.

Among advanced electrode materials, graphene offers excellent electronic, thermal, and mechanical properties that are of interest for a wide variety of applications[8-12]. Due to their ultra-large theoretical specific surface area (2630 m^2 g^{-1}), graphene-based materials may also be promising candidates for advanced catalyst supports. However, the unique lamellar structure of graphene leads to challenges in fabricating an electrode that has both easy charge migration and rapid mass transfer. A large amount of research has been devoted to discovering possible approaches for overcoming this barrier. The creation of hybrid materials, which combine graphene with other nano-materials such as carbon nanotubes/fibers[13], carbon powders[14], conductive polymers nanowires[15, 16], and so forth, to achieve three-dimensional (3D) nano-architectures may be an effective solution since the secondary pores formed between the differently-dimensioned carbons have the potential to act as mass transfer pathways. Alternative structures, such as graphene-based nanoribbons[17], nanomesh[18], or nanoporous materials[19, 20] may also provide channels for mass transport. Furthermore, 3D macroporous graphene[21-24] and vertically-aligned graphene sheets[25] have been shown to provide effective transport channels. However, these architectures can rarely provide pathways for both charge migration and mass transport that are sufficient for the demands of the electrochemical processes that occur within the electrodes of fuel cells. Moreover, the tailored structures produced *via* most of these approaches lack the robustness required to maintain their initial architecture after being packaged into membrane electrode assemblies (MEAs), especially during the ink-painting process used in traditional fabrication methods. As a result, graphene-based materials seldom demonstrate acceptable performance metrics when used in PEMFC electrodes. In contrast to Pt/C-based electrodes, which can attain specific power densities of up to 2-3 W mg^{-1}_{Pt} (for the cathode) and peak power densities of 0.8-1.2 W cm^{-2}, the majority of values reported in the

literature for graphene-supported Pt catalysts used in the oxygen reduction reaction (ORR) are only 1-1.5 W mg^{-1}_{Pt} and 0.3-0.7 W cm^{-2} [26-28]. These results indicate that graphene-based materials have yet to live up to their high potential for fuel cell applications. Hence, the construction of proper electrode architecture is of great important for the further applications of graphene.

Herein, 3D electrode architecture based on a Pt/graphene-Nafion® composite material is for the first time designed and constructed directly on a gas diffusion layer (GDL) *via* a facile freeze-drying/reduction process. Due to the hybridizing effect of the Nafion® ionomers, the electrode possesses a macroporous scaffold structure that enables rapid mass transfer and good proton conduction within the electrode architecture. This collection of pathways for both charges and mass enables enhanced Pt utilization in the composite when used as a PEMFC cathode. As a result, this material demonstrates impressive PEMFC performance, delivering a 2-fold increase in the specific power density as compared to that of a traditional Pt/C cathode and outperforming other reported graphene-based cathodes.

Experimental

Chemicals and synthesis. A dispersion of GO sheets in de-ionized water was prepared from graphite oxide *via* a modified Hummers method. Typically, 50 mg of graphite oxide was dispersed in 100 mL of de-ionized water with continuous ultrasonication for 4 hours, at which point 56 mg of $Pt(NH_3)_2(NO_2)_2$ was added to the dispersion. This mixture stirred at 70 ℃ for 48 hours. Maintaining this temperature, 0.28 g, 0.83 g, 2.50 g and 15.83 g of an aqueous dispersion of Nafion® (10 wt. %, Aldrich) was added to the mixture and stirred for another 6 hours in order to prepare samples with 25%, 50%, 75%, and 95% Nafion® content, respectively. A control sample without Nafion® was also prepared. The mixtures were evaporated to form hybrid slurries with a fixed GO content of 2 wt.%. The slurries were applied onto pieces of a GDL substrate in order to ensure the formation of a smooth, uniform layer with a GO loading of 0.22 mg cm^{-2} (corresponding to a Pt loading of 0.15 mg cm^{-2}). The slurry-coated GDL was then immediately plunged into liquid nitrogen to form hybrid ice, and put into a freeze-drier at -51 ℃ and 7 – 10 Pa for 48 h to sublimate all the ice. Sample Pt(II)/GONMPS was prepared using this procedure and used as a precursor material for the finals steps. The as-prepared Pt(II)/GONMPS was reduced in hydrogen at 250 ℃ for 4 hours, with the resulting samples denoted Pt/GNMPS. The control sample with a lamellar structure was prepared *via* similar procedures, but with the freeze drying process substituted with ambient drying at room temperature. This sample was denoted as Pt/GNL.

Physical characterizations. X-ray diffraction (XRD, D/max-2400X, Ricoh), Raman spectroscopy, field emission scanning electron microscopy (FESEM, JSM-6360LV, JEOL), transmission electron microscopy (TEM, JEM-2011EM, JEOL) and BET tests (QuandraSorb SI4, Quantachrome) were performed on the as-prepared samples. Wetting behaviour was measured using a goniometer (JC2000C1, Shanghai Powereach). The pressure drops experienced by the gas upon passing through the samples were measured with a homemade setup as illustrated in Fig. S5a.

Electrochemical characterization. Electrochemical characterization was conducted in a three-electrode cell with a CHI 760D potentiostat/galvanostat at room temperature (25 ℃). Samples of Pt/GNMPS were peeled off from the GDL substrate for electrochemical testing. Electrodes for electrochemical tests were prepared by loading the catalyst materials onto glassy carbon electrodes with an area of 0.196 cm^2. The sample loadings, as well as that of the commercial 40 wt% Pt-C (JM), were preserved at 51.0 μg_{Pt} cm^{-2}. 0.5 M H_2SO_4 solution, a SCE and a Pt wire were used as the electrolyte, RE, and CE, respectively. Cyclic voltammetry (CV) was performed between 0 and 1.14 V *vs.* RHE at a scan rate of 50 mV s^{-1} under a continuously-purged atmosphere of high purity N_2. ORR polarization curves were obtained using CV tests between 0 and 1.14 V *vs.* RHE at a scan rate of 10 mV s^{-1} in an oxygen-saturated electrolyte.

MEA fabrication and single cell tests. Nafion® 212 membranes (DuPont) were used as the ion-conducting layers. A piece of commercial Pt/C (40 wt.%, JM) loaded GDL was used as the anode (the Pt loading was 0.2 mg cm^{-2}) in all MEAs. The cathodes were the as-prepared Pt/GNMPS-coated GDL, with Pt loadings of 0.15 mg cm^{-2}. MEAs with an active area of 4 cm^2 were fabricated by sandwiching the membrane between the anode and the cathode. Control MEA samples were fabricated with a Pt/GNL cathode or a commercial Pt/C (40 wt.%, JM) cathode with the same Pt loading, respectively. The MEAs were inserted into graphite end plates with serpentine gas flow channels in order to assemble single cell units.

PEMFC performance was evaluated using a Fuel Cell Test Station (Green Light, Inc.) at a cell temperature of 70 ℃ with full humidity. Polarization curves were obtained at a total outlet pressure of 150 kPa on both sides. The anode side was fed with hydrogen with a flow rate of 100 mL min^{-1}, while the cathode side was fed with oxygen with a flow rate of 200 mL min^{-1}.

CV curves between 0 and 1.2 V were recorded with a Solartron SI1287 at 70 ℃ with a scan rate of 50 mV s^{-1}. The anode side was fed with hydrogen with a flow rate of 100 mL min^{-1} and was used as both the reference electrode (RE) and the counter electrode (CE). The cathode side was fed with nitrogen with a flow rate of 100 mL min^{-1} and was used as the working electrode (WE). Inner resistance was measured by electrochemical impedance spectroscopy (EIS) with a Solartron SI1270 under a same condition of performance tests.

Results and Discussion

Structural characterizations. A diagram of the fabrication strategy used to prepare the Pt/graphene-Nafion® composite electrodes can be found in Fig. 1. In brief, graphene oxide (GO) sheets, which had been prepared from graphite oxide using ultrasonic exfoliation, were assembled in combination with a Pt precursor *via* the electrostatic interactions between the oxygen-containing groups of the GO and the Pt cations. These Pt

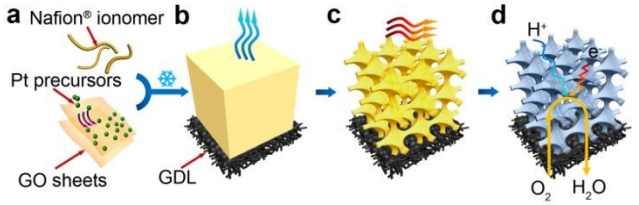

Fig. 1 Schematics for the synthesis strategy used to prepare macroporous scaffolds. (a) Assembly of GO sheets and Pt precursors and preparation of a mixture slurry with Nafion® ionomers. (b) Freeze-drying of the as-prepared slurry. (c) Chemical reduction with hydrogen flow. (d) ORR process testing with the as-prepared cathode.

cation-decorated sheets were then mixed with Nafion® ionomers to make an aqueous suspension. The mixed slurry was spread onto a GDL (Fig. 2a) before being rapidly plunged into liquid nitrogen in order to create tiny ice crystals within the suspension. Then the drying process maintains an inverse phase of ice as the macroporous scaffold after the sublimation (Fig. 2b)[29-33]. After heat treatment at 250 ℃ in a hydrogen atmosphere, the Pt precursor and GO sheets were reduced to metallic Pt and graphene respectively, which can be observed in the blackening of the (previously brown) GO layer (Fig. 2c). As-prepared samples made using this procedure, which are hereafter referred to as Pt/GNMPS (Pt/graphene-Nafion® macroporous scaffold), can be directly used as cathodes for PEMFC. Notably, this method of fabricating electrodes is very amenable to scale-up.

The cross-section of a typical sample made with a Nafion® content of 50% (Fig. 2d; see Experimental section for compositional details) reveals the macroporous structure of the catalyst layer, which is approximately 140 μm in thickness, or 28-fold thicker than a lamellar graphene structure with the same mass loading (Pt/GNL, Fig. S1), indicating a significant fraction (more than 95%) of the scaffold structure consists of pore volume. BET surface area of the Pt/GNMPS-50 sample is 21.6 $m^2 g^{-1}$, which is significantly increased compared with 3.9 $m^2 g^{-1}$ for the layered sample (Pt/GNL). A porous morphology with typical pore sizes of approximately 3-5 μm can be observed in the top view (Fig. 2e). Interestingly, one implication of this macroporous structure is that the catalyst layer is more strongly hydrophobic (Fig. 2e, inset) than the lamellar sample (Fig. S1, inset). The close-up view of the cross-sectional morphology (Fig. 2g) shows a similar pore structure to that of the top surface (Fig. 2e), suggesting that the scaffold pore structure is isotropic. Meanwhile, high-magnification SEM imagery of the edge of the sample (Fig. 2h) shows inter-tangled graphene nano-sheets with a well-known wrinkle morphology[34, 35]. TEM images of the as-prepared scaffold (Fig. 2i) demonstrate that Pt nanoparticles (NPs) with an average particle size of 2.69 nm are loaded ultra-homogenously on the graphene sheets.

The morphology and structure of Pt/GNMPS electrodes are easily modified by simply varying the mass ratio of Nafion® ionomers to GO in the composite. In the absence of Nafion® (Fig. 3a and f), it is difficult for the pore structure to form on the top surface, while only random stacks of graphene sheets are observed in the cross-sectional view. Upon introducing the Nafion® ionomers, however, pores appear on the top surface (Fig. 3b-e) as well as throughout the cross section (Fig. 3g-j). By increasing the mass ratio of Nafion® to GO, the average pore size can expanded from approximately 3 μm to nearly 20 μm (Fig. 3k-o), while simultaneously smoothing the wrinkled

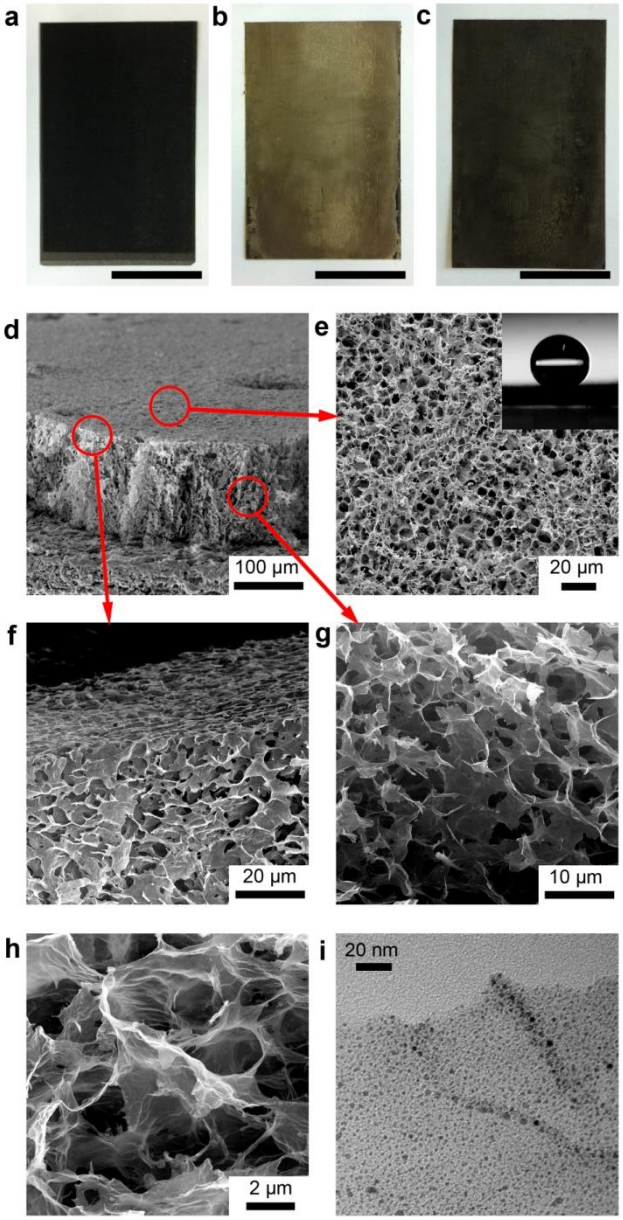

Fig. 2 Morphological images of a typical Pt/GNMPS. (a-c) Optical photographs of different synthesis stages; scale bar is 5 cm. (d) An SEM micrograph of a cliff-like edge in a sample of Pt/GNMPS. (e) SEM imagery of the top surface, inset is the water wetting behavior as tested on this surface. (f) Close-up SEM of the edge. (g) SEM image of the cross section. (h) High-magnification SEM of the cross section view. (i) TEM image of Pt NPs supported on graphene sheets.

graphene surfaces. The agglomeration experienced by Nafion® ionomers in water leads to a tendency to form a scaffold structure with considerable pore sizes. In contrast, the two dimensional structure and abundant amount of oxygen-containing groups of the GO nano-sheets predisposes them to the development of puffy stacks or interlocked layers, especially at phase boundaries[36, 37], resulting in relatively small and disordered pores. The combination of these two behaviors may lead to the gradual change in the scaffold structures of the composites.

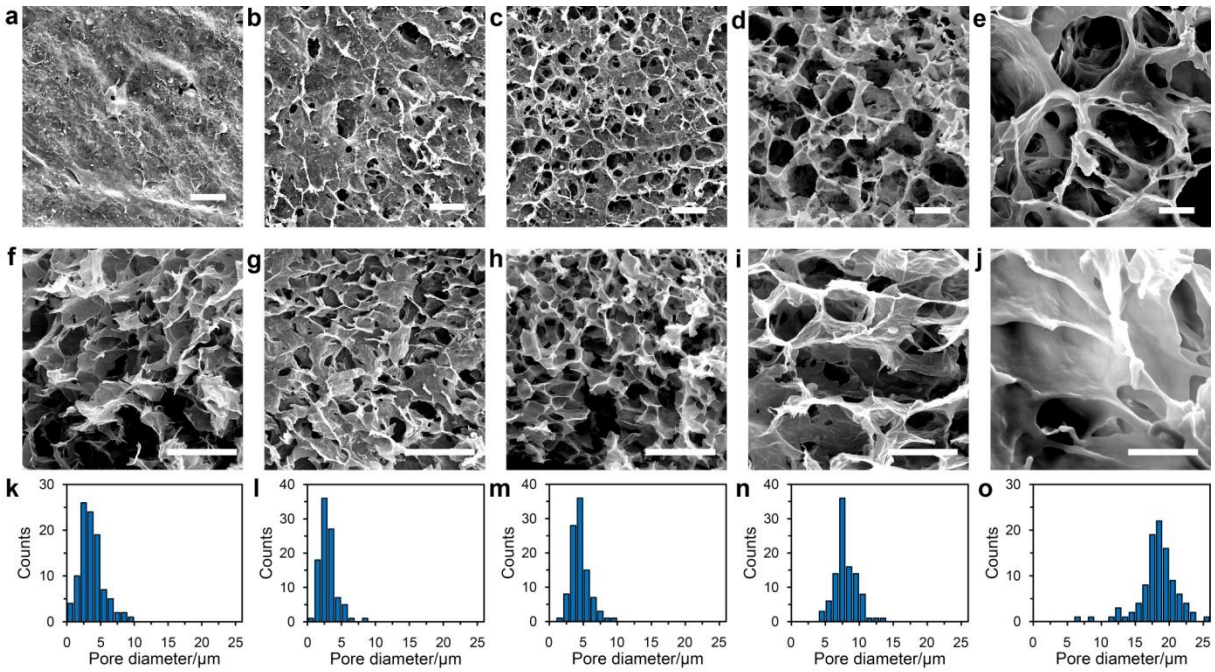

Fig. 3 Morphological comparison of the macroporous scaffolds with varied Nafion® contents. (a-e) SEM images of the top surface of Pt/GNMPS with Nafion® contents of 0, 25%, 50%, 75% and 95%, respectively. The scale bar is 20 μm. (f-j) Corresponding cross-sectional SEM images. The scale bar is 10 μm. k-o, Histograms of sample pore size distributions as derived from f-j.

X-ray diffraction (XRD) and Raman spectroscopy were used to study the crystal structures of the composite scarffolds. The diffraction peaks found in the XRD patterns of metallic Pt (Fig. 4a) embedded in samples with different Nafion® contents are similar to one another, indicating a constant distribution of Pt particle sizes, which is in agreement with the TEM results found in Fig. S2. The peaks located at approximately 17 ° are attributed to GO and Nafion® agglomerates, given the similar interplanar distances for both GO sheets and the PTFE backbones of the Nafion®[38-40]. The intensity of the peak found around 22-26 °, which can be assigned to the (002) face of graphite, increases with decreasing Nafion® content, suggesting increased graphitization of GO.

This variation in the degree of graphitization with Nafion® content in the scaffold can also be observed in the Raman spectra of the samples (Fig. 4b and c). Prominent carbon D and G bands (Fig. 4b) are apparent in all spectra, but the ratio of the D/G intensity varies. The value of I_D/I_G calculated from the spectrum of a post-hydrogen reduction process sample with 50% Nafion® content (curve 3) is significantly increased as compared with that of a similar sample before reduction (curve 6), indicating a decrease in sp^2 domains. This phenomenon is consistent with previously-reported results concerning the chemical reduction of GO, which explain the decrease in sp^2 domains observed in the GO after reduction by citing the simultaneous decrease in the sizes and increase in the number of graphene nano-sheets present[41]. For samples with high Nafion® contents (75% and 95%), the encapsulation effect provided by the Nafion® may act to prevent the intensive reduction of the GO sheets, thereby resulting in lower I_D/I_G values. By contrast, the decrease in the I_D/I_G values seen for samples with low Nafion® contents (0 and 25%) is due to the significant graphitization of the graphene layers in these samples, and is due to the abundant number of sp^2 domains within the graphitized samples. The increase in the extent of graphitization with decreasing Nafion® contents in the composite scaffolds is also reflected in the 2D bands, as shown in Fig. 4c. As previously reported, single-layer graphene exhibits a pominent 2D peak located at approximately 2680 cm^{-1}, while graphite has one weak $2D_1$ peak at 2680 cm^{-1} and a prominent $2D_2$ peak at 2720 cm^{-1}. As the number of graphene layers increases, the features of the 2D band evolve from a single peak to a convolution of the two peaks of graphite[42, 43]. Such an evolution can be clearly observed in the 2D bands of the samples with low Nafion® contents (Fig. 4c, curves 1-5), indicating the increase in graphitization of the graphene layers in these samples. These results suggest that the extent of graphitization of the porous structures can be tailored simply by altering the Nafion® content of the composites, without significant effects on the Pt particle size.

PEMFC single cell tests. Pt/GNMPS samples with different Nafion® contents were tested as the cathodes in single-cell PEMFC devices, with the results shown in Fig. 5a. The best performance was obtained using a sample that contained a Nafion® content of 50%, with a peak power density of 0.93 W cm^{-2} (Table 1). By contrast, the performance of a cell made using a cathode with no Nafion® (sample Pt/GNMPS-0) exhibited poor performance, with a peak power density of only 0.12 W cm^{-2}. Increasing the Nafion content to over 50%, also led to decreases in cell performance.

The use of a 50% Nafion® cathode with a macroporous scaffold structure also led to a six-fold increase in peak power density as compared with lamellar cathode with the same composition (sample Pt/GNL-50). Furthermore, the performance of sample Pt/GNMPS-50 was found to be a significant improvement over a commercial Pt/C catalyst layer on GDL with the same Pt loading (0.15 mg cm^{-2}). The mass specific power density of a device made with sample Pt/GNMPS-50 was measured to be 6.2 W mg^{-1}_{Pt}, while the device that was fabricated with a commercial Pt/C catalyst demonstrated only 5.2 W mg^{-1}_{Pt}. The performance obtained for

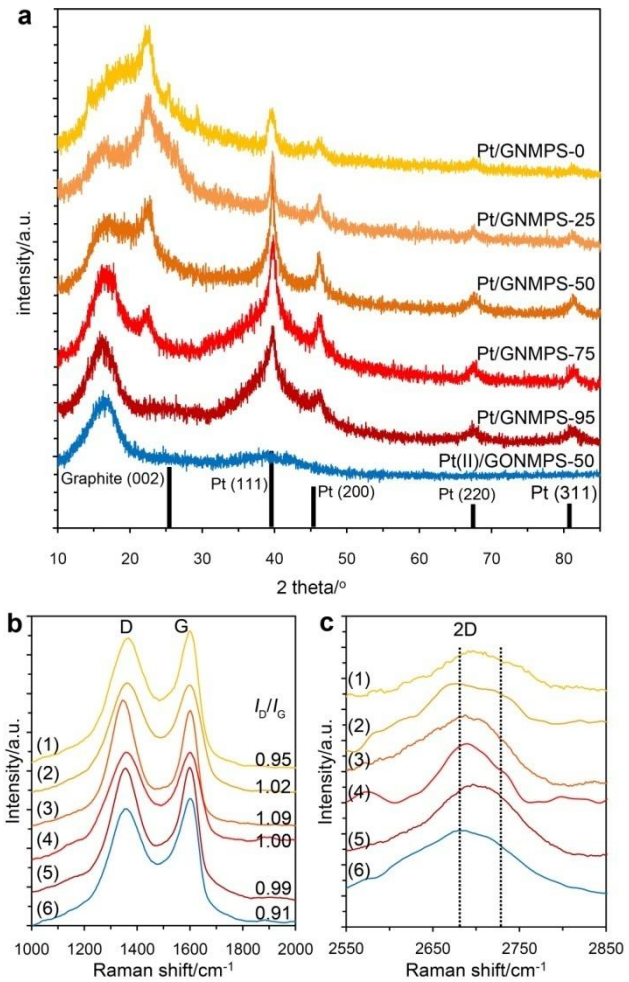

Fig. 4 XRD patterns (a) and Raman spectra (b, c). The numbers 1-6 represent samples Pt/GNMPS-0, Pt/GNMPS-25, Pt/GNMPS-50, Pt/GNMPS-75, Pt/GNMPS-95, and Pt(II)/GONMPS-50, respectively.

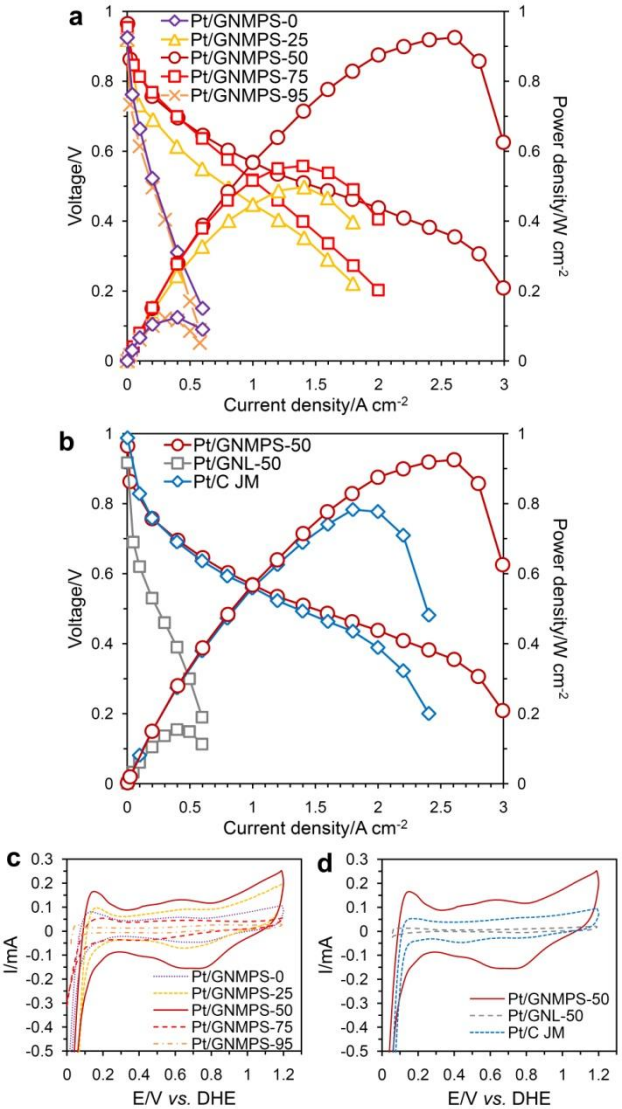

Fig. 5 PEMFC single cell test results. (a-b) Polarization curves of different samples used as cathodes. (c-d) CV curves measured using different cathodes and a 50 mV s^{-1} scan rate. The anode was fed with 50 mL min^{-1} H_2, and the cathode was supplied with 100 mL min^{-1} N_2. The temperature was 70 ℃.

the macroporous cathode surpasses most of the values reported for graphene-based electrodes with a relatively low Pt loadings, and is also competitive with the low-Pt fuel cell technologies that are currently being researched[44].

To explore the mechanism behind this improvement in the performance of single-cell devices made with the novel electrode described here, the electrochemical properties of the electrode materials were measured using a rotation disk electrode (RDE) in 0.5 M H_2SO_4 electrolyte. Cyclic voltammograms (CV; Fig. S3) reveal that all of the macroporous scaffolds have relatively similar electrochemical surface areas (ECSAs), with values of approximately 75-95 m^2 g^{-1}_{Pt}. This result may be due to the similar average sizes of the Pt particles decorated on the graphene sheets (Fig. S2). The ORR onset potential was also similar for all samples, at approximately 1.03 V (*vs.* RHE) (Fig. S4). Only a slight decline in performance was observed for the samples with higher Nafion® contents when operated in the regions in which mass transport polarization was dominant. These results indicate that the catalysts show similar catalytic activity for the ORR, and thus that the significant differences in device performance seen with different PEMFC samples can be attributed to the structural variations in the electrode.

Further tests were conducted to measure the mass transport and charge migration behaviors within the novel electrode architectures in order to elucidate the detailed causes of the differences in cell performance. Mass transport behavior within the electrodes was examined by measuring the difference in pressure of a gas before and after penetrating through the electrode layer (Fig. S5). As expected, the resistance to mass transport was smaller for the electrodes with larger pores (Fig. 6b), and thus the pressure difference was measured to be smaller in the samples with larger Nafion® contents, as shown in Fig. 6a (red dot).

The increase in the internal resistances of the single cell devices (Fig. 6a, green diamonds) is due to discontinuities in the electron conduction pathways. These discontinuities form when the contact between graphene sheets is interrupted by the presence of large amounts of Nafion®. However, the high electronic conductivity of graphene means that the internal

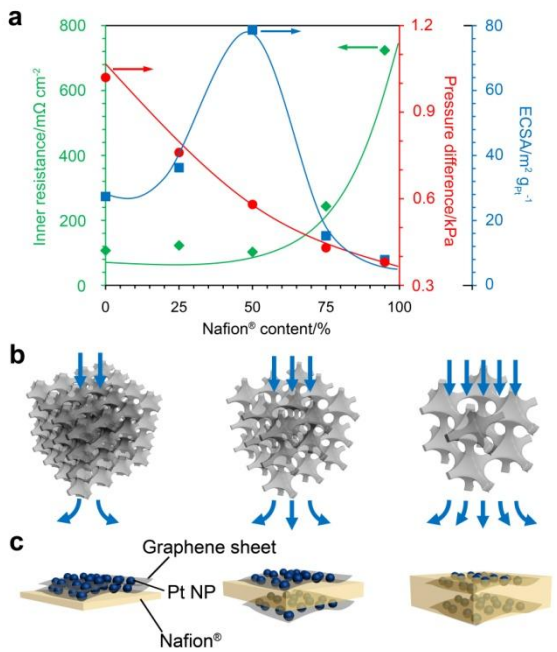

Fig. 6 Variation of electrode behavior with scaffold structure. (a) Curves showing the dependence on Nafion® content of the internal cell resistances (diamonds), gas pressure differences (circles), and cathode ECSAs (squares). (b) Schematics of mass transport within the different scarffold structures. (c) Schematic of Pt/graphene embedded in Nafion®.

resistances of the cells made with Nafion® contents below 50% are almost equal to that of a traditional cell with a Pt/C cathode (Table 1), even though the thickness of the novel catalyst scaffold layer is ten times that of the conventional catalyst layer. The migration of protons within the electrode is a critical determinant of the amount of hydrogen adsorption/desorption that can occur on the Pt surface. Therefore, the calculated ECSA values for the Pt within the cathodes (Fig. 5c and Table 1) exhibit a volcano-like trend with increasing Nafion® contents, as shown in Fig. 6a (blue squares). This result may be explained by the structural change shown in Fig. 6c. When insufficient Nafion® is present to prevent aggregation of the graphene, the graphene layers tend to stack as evidenced by XRD and Raman results. As a result, some Pt NPs are buried beneath the graphene layers and are therefore inaccessible for catalytic activity. Too much Nafion® in the structure, however, might encapsulate the graphene domains, also cutting off access to the Pt NPs. Such a balance controlled by graphene stacking and Nafion filling/blocking could also be evidenced by the BET surface area results as shown in Table S1. By adding an optimized amount of Nafion®, a structure that is suitable for proton migration while also exposing the maximum amount of Pt NPs may be accomplished.

The advantages of this highly-effective electrode architecture are overwhelming. By adding Nafion® ionomers, the ultra-large surface area of the graphene sheets can be fully unwrapped, creating a macroporous scaffold structure. The graphene is able to accociate with Pt NPs to form electrochemical active sites, which act as triple phase boundaries. This is reflected in the enhanced ECSA values obtained for the MEAs as compared with those of the lamellar graphene structure and the traditional Pt/C electrode, as shown in Fig. 5d. The extent of Pt utilization (the ratio of ECSA to geometric surface area) is also significantly improved in this novel electrode, with a maximum value of 76% as compared to 28% for a conventional electrode (Table 1). Furthermore, the extremely high pore volume and the macro-scale pore sizes lead to improved mass transport as well as resulting in enhanced single cell performance. In sum, the elaborate design of pathways for charge migration and mass transport that can be accomplished using the synthetic technique described above leads to highly effective cathode design for the ORR.

Conclusion

In this work, an electrode architecture with a macroporous scaffold based on a Pt/graphene-Nafion® composite was introduced. The morphology of the composites could be easily controlled by simply altering the Nafion® content. When used as PEMFC cathodes, the electrodes exhibit a range of performances due to variations in the pathways for charge (electron/proton) migration and mass (gas/liquid) transport. The optimized structure (Pt/GNMPS-50) shows excellent performance, with a peak power density of 0.93 W cm^{-2} and a mass specific power density of 6.2 W mg^{-1}_{Pt}, values which are 6-fold greater than those demonstrated by a lamellar structure with the same composition and 1.2-fold greater than a commercial Pt/C coated electrode with the same Pt loading. This performance represents a significant breakthrough in overcoming the inconvenient nature of graphene, while also being comparable to the most advanced architectures used for fuel cell electrodes. The excellent behavior demonstrated here

Table 1. Characteristic parameters of PEMFCs with different samples as cathodes.

Samples	Peak power density (W cm^{-2})	Cathode specific mass activity[a] (W mg^{-1}_{Pt})	ECSA in MEA (m^2 g^{-1}_{Pt})	Pt utilization[b] (%)	Inner resistance (Ω cm^2)
Pt/GNMPS-0	0.12	0.80	27	33	0.11
Pt/GNMPS-25	0.50	3.3	36	38	0.12
Pt/GNMPS-50	0.93	6.2	79	76	0.10
Pt/GNMPS-75	0.56	3.7	15	17	0.24
Pt/GNMPS-95	0.12	0.81	7.9	8.2	0.72
Pt/GNL-50	0.15	1.0	9.3	9.7	0.39
Pt/C JM	0.78	5.2	26	28	0.09

[a] The data are based on the Pt loading of 0.15 mg cm^{-2} for each sample.
[b] Pt utilizations are the ratios of ECSAs to geometric surface areas of the spherical Pt NPs with diameters from Fig. S3; Pt NP size of commercial Pt/C (40%, JM) is adopted as 3.0 nm.

can be attributed to the high Pt utilization and the enhanced mass transport that arises from the tailored structure of the transport pathways. The fact that the novel electrodes described here have better performance than conventional electrodes despite being ten times thicker contradicts the conventional wisdom which states that thinner catalyst layers will lead to better mass transport in electrodes. As such, this work can provide insights for the further design of novel electrodes for fuel cells or other electrochemical devices, such as lithium ion batteries, super capacitors, metal-air batteries, and so forth and may also inspire future developments of micro/nano-technologies.

Acknowledgements

This work is financially supported by the National Basic Research Program of China (2012CB215500), the "Strategic Priority Research Program" of the Chinese Academy of Sciences (XDA09030104) and National High-tech R&D Programme (No. 2012AA053401).

Notes and references

[a] *Division of Fuel Cell & Battery, Dalian National Laboratory for Clean Energy, Dalian Institute of Chemical Physics, Chinese Academy of Sciences, Dalian 116023, China. Fax: 86-411-84379797; Tel: 86-411-84379063; E-mail: gqsun@dicp.ac.cn*

[b] *University of Chinese Academy of Sciences, Beijing 100039, China.*

Electronic Supplementary Information (ESI) available: SEM and TEM images, CV and ORR curves, schematic and results of pressure difference tests.. See DOI: 10.1039/b000000x/

1. M. K. Debe, *Nature*, 2012, 486, 43-51.
2. B. C. Steele and A. Heinzel, *Nature*, 2001, 414, 345-352.
3. E. Ticianelli, C. Derouin, A. Redondo and S. Srinivasan, *J. Electrochem. Soc.*, 1988, 135, 2209-2214.
4. S. Lee, S. Mukerjee, J. McBreen, Y. Rho, Y. Kho and T. Lee, *Electrochim. Acta*, 1998, 43, 3693-3701.
5. S. Litster and G. McLean, *J. Power Sources*, 2004, 130, 61-76.
6. C.-Y. Wang, *Chem. rev.*, 2004, 104, 4727-4766.
7. A. Bonnefont, P. Ruvinskiy, M. Rouhet, A. Orfanidi, S. Neophytides and E. Savinova, *Wiley Interdisciplinary Reviews: Energy and Environment*, 2014.
8. K. S. Novoselov, A. K. Geim, S. V. Morozov, D. Jiang, Y. Zhang, S. V. Dubonos, I. V. Grigorieva and A. A. Firsov, *Science*, 2004, 306, 666-669.
9. A. K. Geim and K. S. Novoselov, *Nat. Mater.*, 2007, 6, 183-191.
10. H.-J. Choi, S.-M. Jung, J.-M. Seo, D. W. Chang, L. Dai and J.-B. Baek, *Nano Energy*, 2012, 1, 534-551.
11. J. Liu, C. K. Poh, D. Zhan, L. Lai, S. H. Lim, L. Wang, X. Liu, N. G. Sahoo, C. Li, Z. Shen and J. Lin, *Nano Energy*, 2013, 2, 377-386.
12. J. Liu, L. Lai, N. G. Sahoo, W. Zhou, Z. Shen and S. H. Chan, *Australian J. Chem.*, 2012, 65, 1213-1222.
13. B. P. Vinayan and S. Ramaprabhu, *Nanoscale*, 2013, 5, 5109-5118.
14. D. P. He, K. Cheng, T. Peng and S. C. Mu, *J. Mater. Chem. A*, 2013, 1, 2126-2132.
15. C. Wang, Y. Wang, J. Graser, R. Zhao, F. Gao and M. J. O'Connell, *Acs Nano*, 2013, 7, 11156-11165.
16. Q. Wu, Y. Xu, Z. Yao, A. Liu and G. Shi, *Acs Nano*, 2010, 4, 1963-1970.
17. C. Zhang, Z. Peng, J. Lin, Y. Zhu, G. Ruan, C.-C. Hwang, W. Lu, R. H. Hauge and J. M. Tour, *Acs Nano*, 2013, 7, 5151-5159.
18. J. Bai, X. Zhong, S. Jiang, Y. Huang and X. Duan, *Nat. Nanotechnol.*, 2010, 5, 190-194.
19. D. E. Jiang, V. R. Cooper and S. Dai, *Nano Lett.*, 2009, 9, 4019-4024.
20. J. Xiao, D. Mei, X. Li, W. Xu, D. Wang, G. L. Graff, W. D. Bennett, Z. Nie, L. V. Saraf, I. A. Aksay, J. Liu and J.-G. Zhang, *Nano Lett.*, 2011, 11, 5071-5078.
21. L. Estevez, A. Kelarakis, Q. M. Gong, E. H. Da'as and E. P. Giannelis, *J. Am. Chem. Soc.*, 2011, 133, 6122-6125.
22. S. Y. Yin, Z. Q. Niu and X. D. Chen, *Small*, 2012, 8, 2458-2463.
23. C. Li and G. Q. Shi, *Nanoscale*, 2012, 4, 5549-5563.
24. V. Chabot, D. Higgins, A. Yu, X. Xiao, Z. Chen and J. Zhang, *Energ. Environ. Sci.*, 2014, 7, 1564-1596.
25. J. R. Miller, R. A. Outlaw and B. C. Holloway, *Science*, 2010, 329, 1637-1639.
26. B. Seger and P. V. Kamat, *J. Phys. Chem. C*, 2009, 113, 7990-7995.
27. B. P. Vinayan, R. Nagar, N. Rajalakshmi and S. Ramaprabhu, *Adv. Funct. Mater.*, 2012, 22, 3519-3526.
28. B. P. Vinayan, R. Nagar and S. Ramaprabhu, *J. Mater. Chem.*, 2012, 22, 25325-25334.
29. H. F. Zhang, I. Hussain, M. Brust, M. F. Butler, S. P. Rannard and A. I. Cooper, *Nat. Mater.*, 2005, 4, 787-793.
30. M. C. Gutierrez, M. L. Ferrer and F. del Monte, *Chem. Mat.*, 2008, 20, 634-648.
31. S. Deville, E. Saiz, R. K. Nalla and A. P. Tomsia, *Science*, 2006, 311, 515-518.
32. C. A. L. Colard, R. A. Cave, N. Grossiord, J. A. Covington and S. A. F. Bon, *Adv. Mater.*, 2009, 21, 2894-2898.
33. S. Ansari, A. Kelarakis, L. Estevez and E. P. Giannelis, *Small*, 2010, 6, 205-209.
34. M. J. McAllister, J. L. Li, D. H. Adamson, H. C. Schniepp, A. A. Abdala, J. Liu, M. Herrera-Alonso, D. L. Milius, R. Car, R. K. Prud'homme and I. A. Aksay, *Chem. Mat.*, 2007, 19, 4396-4404.
35. H. C. Schniepp, J. L. Li, M. J. McAllister, H. Sai, M. Herrera-Alonso, D. H. Adamson, R. K. Prud'homme, R. Car, D. A. Saville and I. A. Aksay, *J. Phys. Chem. B*, 2006, 110, 8535-8539.
36. D. A. Dikin, S. Stankovich, E. J. Zimney, R. D. Piner, G. H. B. Dommett, G. Evmenenko, S. T. Nguyen and R. S. Ruoff, *Nature*, 2007, 448, 457-460.
37. C. Chen, Q.-H. Yang, Y. Yang, W. Lv, Y. Wen, P.-X. Hou, M. Wang and H.-M. Cheng, *Adv. Mater.*, 2009, 21, 3007-3012.
38. L. H. Tang, Y. Wang, Y. M. Li, H. B. Feng, J. Lu and J. H. Li, *Adv. Funct. Mater.*, 2009, 19, 2782-2789.
39. G. Gebel, P. Aldebert and M. Pineri, *Macromolecules*, 1987, 20, 1425-1428.

40. T. D. Gierke, G. E. Munn and F. C. Wilson, *J. Polym. Sci. Pt. B-Polym. Phys.*, 1981, 19, 1687-1704.
41. S. Stankovich, D. A. Dikin, R. D. Piner, K. A. Kohlhaas, A. Kleinhammes, Y. Jia, Y. Wu, S. T. Nguyen and R. S. Ruoff, *Carbon*, 2007, 45, 1558-1565.
42. D. Graf, F. Molitor, K. Ensslin, C. Stampfer, A. Jungen, C. Hierold and L. Wirtz, *Nano Lett.*, 2007, 7, 238-242.
43. A. C. Ferrari, J. C. Meyer, V. Scardaci, C. Casiraghi, M. Lazzeri, F. Mauri, S. Piscanec, D. Jiang, K. S. Novoselov, S. Roth and A. K. Geim, *Phys. Rev. Lett.*, 2006, 97, 4.
44. A. Brouzgou, S. Song and P. Tsiakaras, *Appl. Catal. B Environ.*, 2012, 127, 371-388.

